

Comparison study of counting and fitting methods in search for neutrinoless double beta decays*

Hao-Yang Fu,^{1,2} Wen-Tai Luo,^{1,2,†} Xiang-Pan Ji,³ and Shao-Min Chen^{1,2,4}

¹Department of Engineering Physics, Tsinghua University, Beijing, China

²Center for High Energy Physics, Tsinghua University, Beijing, China

³School of Physics, Nankai University, Tianjin, China

⁴Key Laboratory of Particle & Radiation Imaging, Tsinghua University, Ministry of Education, Beijing, China

In the search for neutrinoless double beta decay ($0\nu\beta\beta$) experiments, common methods for sensitivity calculations include the counting method and the spectrum fitting method. This research compares their difference in sensitivity under various energy resolutions. Additionally, the performance of high and low Q -value $0\nu\beta\beta$ isotopes is compared. The results of this research could provide guidance on the choice of methods for sensitivity calculations, energy resolution and $0\nu\beta\beta$ isotopes for future $0\nu\beta\beta$ experiments.

Keywords: Neutrinos, Neutrinoless double-beta decay, MC simulation, Analysis and statistical methods

I. INTRODUCTION

Neutrinoless double beta decay ($0\nu\beta\beta$), $(A, Z) \rightarrow (A, Z+2)+2e^-$, is an extremely rare decay process that occurs in certain nuclides [1]. The investigation of $0\nu\beta\beta$ plays a significant role in exploring physics beyond the standard model [2]. The half-life of $0\nu\beta\beta$ could also provide crucial information for determining the neutrino mass hierarchy, since the effective mass of Majorana neutrinos $\langle m_{\beta\beta} \rangle$ is highly related to the half-life. The existence of $0\nu\beta\beta$ decay would demonstrate that neutrinos are Majorana fermions.

Currently, there is no confirmed experimental evidence for neutrinoless double beta decay. Extensive experimental efforts are being dedicated to the search for $0\nu\beta\beta$ [3–13]. These experimental studies typically employ two methods to estimate the sensitivity to the half-life of $0\nu\beta\beta$. One is the counting method, which involves statistical analysis of events within a selected region of interest (ROI). The counting method relies on the number of events in the ROI. The other is the fitting method, which utilizes spectrum fitting to calculate the sensitivity. Despite the fact that the fitting method requires a detailed study of the background, it is capable of utilizing information from events outside the ROI. This research examined the differences in sensitivity between the two methods.

Currently, the best results in $0\nu\beta\beta$ experiments have come from the KamLAND-Zen experiment using a liquid scintillator detector [12], which has the advantage of high exposure to $0\nu\beta\beta$ nuclei. In this study, we chose to simulate a liquid scintillator detector as an example for our study. The detector simulations were performed with an energy resolution δ (defined by the standard deviation σ_E at 1 MeV as $\delta = \frac{\sigma_E}{1\text{MeV}}$) ranging from 1% to 7%. This made the conclusion of this research applicable to other detector types in this energy resolution range, such as time projection chamber (TPC) detectors.

Furthermore, the studied isotopes in this research were selected as ^{150}Nd and ^{130}Te . These isotopes represent the high Q -value (approximately 3.37 MeV) and low Q -value

(approximately 2.53 MeV) isotopes. The purpose of this research is to provide guidance for future experiments using various isotopes in the selection of appropriate methods for sensitivity calculations.

Section II describes the simulation setup. Section III presents the background of this research. Section IV provides a detailed description of the counting and fitting methods, together with a comparison of their results. Section V presents a discussion, and Section VI concludes.

II. DETECTOR SETUP AND SIMULATION

A. Detector setup

The geometry of the liquid scintillator detector used in this research is similar to JUNO [14]. The general structure of the multi-hundred-ton detector is shown in Fig. 1. The main body of the detector is a 500-ton liquid scintillator enclosed in a 5-meter-radius acrylic sphere. The acrylic sphere is wrapped around by the mineral oil. There is a stainless steel support frame for the photomultiplier tubes (PMT) at a radius of 6 meters. Thousands of 8-inch PMTs are placed on the support frame. The outer layer is a cubic water tank with a side length of 12 meters.



Fig. 1. A simple concept graphic of the detector geometry used in simulations.

In this research, the liquid scintillator is loaded with $0\nu\beta\beta$ isotopes by a specific mass fraction. This fraction is set to be 1% for natural Nd and Te [15–17], which corresponds to a mass of 0.285 ton for ^{150}Nd and 1.71 ton for ^{130}Te .

* Supported by the National Natural Science Foundation of China (12127808).

† Corresponding author, luowt@mail.tsinghua.edu.cn

B. Simulation

The detector simulations used a simulation package named Jinping Simulation and Analysis Package (JSAP). The JSAP is based on GEANT4 and has some features, which include the generator, detector simulation, dark noise and pre-trigger, waveform generation, and trigger. The details of JSAP were described in [18].

III. NEUTRINOLESS DOUBLE BETA DECAY EXPERIMENT BACKGROUNDS

The $0\nu\beta\beta$ experiment backgrounds have various sources, including two-neutrino double beta decay ($2\nu\beta\beta$), solar neutrinos, radioactive and cosmogenic backgrounds. These backgrounds will mask the $0\nu\beta\beta$ signals. The simulations in this research are based on the China Jinping Underground Laboratory (CJPL). At the CJPL, the cosmic ray flux and the cosmogenic background are one-thousandth of those in the KamLAND-Zen experiment [19, 20], causing them to be negligible. In this research, only the $2\nu\beta\beta$, solar neutrino, and radioactive backgrounds are considered.

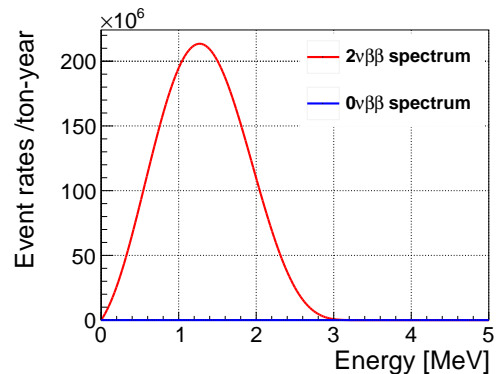
A. Two-neutrino double beta decay background

The $2\nu\beta\beta$ is an intrinsic background in $0\nu\beta\beta$ experiments. Similar to the $0\nu\beta\beta$ reaction, the $2\nu\beta\beta$ reaction, $(A, Z) \rightarrow (A, Z + 2) + 2e^- + 2\bar{\nu}_e$, generates a background through the energy deposition of the two electrons in the final state. Since the anti-electron neutrinos in the final state can take away energy, the total kinetic energy of two electrons forms a continuous spectrum, with its endpoint being the reaction's Q -value. This energy spectrum can be approximately given by [21]

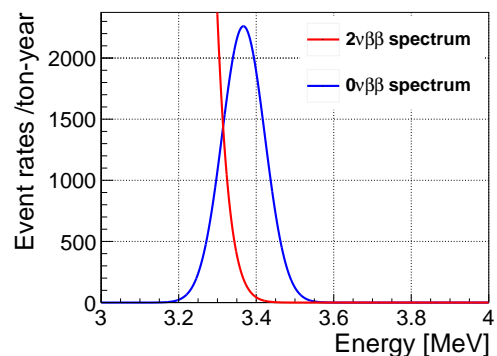
$$\frac{dN}{dK} \approx (K - Q)^5 \left(1 + 2K + \frac{4}{3}K^2 + \frac{1}{3}K^3 + \frac{1}{30}K^4 \right), \quad (1)$$

where K is the total kinetic energy of the two final state electrons and Q is the reaction's Q -value. This equation neglects the effect of double Fermi transitions and uses the Interaction Boson Model with the closed approximation, while the Fermi factor is computed using the Primakoff-Rosen approximation [22].

Fig. 2 shows the $2\nu\beta\beta$ and $0\nu\beta\beta$ two-electron total kinetic energy spectra with an energy resolution of $3\%/\sqrt{E(\text{MeV})}$ for ^{150}Nd . The ratio of the half-life of $2\nu\beta\beta$ to the half-life of $0\nu\beta\beta$ is set to be $1:10^6$, since the ratio of the half-life of $2\nu\beta\beta$ to the lower limit of the half-life of $0\nu\beta\beta$ in the KamLAND-Zen experiment is approximately $1:10^5$ [11].



(a)



(b)

Fig. 2. The full view (a) and the enlarged view (b) of two-electron total kinetic energy spectra of $2\nu\beta\beta$ and $0\nu\beta\beta$, obtained with an energy resolution of $3\%/\sqrt{E(\text{MeV})}$. The ratio of the half-life of $2\nu\beta\beta$ to the half-life of $0\nu\beta\beta$ is set to be $1:10^6$.

B. Solar neutrino background

Solar neutrinos are produced through nuclear fusion processes occurring in the core of the Sun. For most nuclides of interest in the $0\nu\beta\beta$ experiments, the Q -value falls within the region of >2.4 MeV [2]. Within this energy range, only the ^8B and the hep neutrinos exhibit significant contributions [23]. Since the ^8B component is approximately hundreds of times higher than the hep component, the contribution of the hep component of solar neutrinos is ignored in this research.

1. Neutrino-electron elastic scattering

The primary mechanism by which solar neutrinos contribute to the background in the $0\nu\beta\beta$ experiments is through elastic scattering (ES). Theoretical studies can provide the survival probabilities of solar neutrinos reaching Earth [24]. The flux of solar neutrinos $\frac{d\phi_i(E_\nu)}{dE_\nu}$, where $i = e, \mu, \tau$, can be calculated using these survival probabilities. By combining this flux with the neutrino-electron elastic scattering cross-

sections $\frac{d\sigma_i(E_e, E_\nu)}{dE_e}$ [25], the recoil electron spectrum can be derived as

$$\frac{dN_e(E_e)}{dE_e} = N_0 \times t \times \sum_i^{\text{flavours}} \int dE_\nu \frac{d\phi_i(E_\nu)}{dE_\nu} \frac{d\sigma_i(E_e, E_\nu)}{dE_e}, \quad (2)$$

where N_0 is the number of electrons in the target and t is the measuring time.

As a result, the ${}^8\text{B}$ recoil electron spectrum with $3\%/\sqrt{E(\text{MeV})}$ energy resolution is shown in Fig. 3.

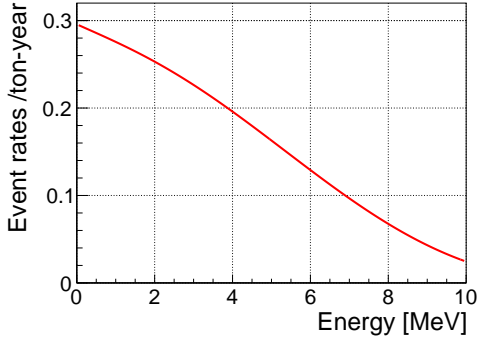
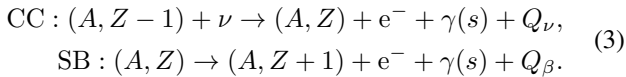


Fig. 3. The neutrino-electron elastic scattering electron recoil spectrum of ${}^8\text{B}$ neutrinos, obtained with an energy resolution of $3\%/\sqrt{E(\text{MeV})}$.

2. Decay nuclide capture background

Neutrinos can be captured by nuclides in the detector through a charged current (CC) process. Ref. [26, 27] indicates that the $0\nu\beta\beta$ nuclide would capture neutrinos and then undergo the single β decay (SB) to release an electron (and possibly photons):



This research follows the calculations from [26, 27] to obtain the energy spectrum of β or $\beta + \gamma$. For example, ${}^{150}\text{Nd}$ undergoes the CC process to become ${}^{150}\text{Pm}$. Subsequently, ${}^{150}\text{Pm}$ undergoes the SB process to the ground state or excited states of ${}^{150}\text{Sm}$. This process would emit an electron and probably de-excitation photons. The calculation considers all decay paths of ${}^{150}\text{Pm}$ with a branching ratio greater than 1% and sets the lower limit of the branching ratio for the ground state at 10%. This calculation results in a total branching ratio of 99.7%. The energy spectrum of β decay used here is approximately given by [28]

$$\frac{dN}{dE} \approx (E_0 - E_e)^2 E_e p_e F(Z, E_e), \quad (4)$$

where E_0 is the energy of the β decay endpoint, E_e and p_e are the energy and momentum of the final state electron, and $F(Z, E_e)$ is the Fermi function.

${}^{130}\text{Te}$ follows a similar process, undergoing the CC process to transform into ${}^{130}\text{I}$, which subsequently undergoes the SB process to convert into ${}^{130}\text{Xe}$. Fig. 4 provides the total energy spectra of the capture of neutrinos by ${}^{150}\text{Nd}$ and ${}^{130}\text{Te}$, with an energy resolution of $3\%/\sqrt{E(\text{MeV})}$.

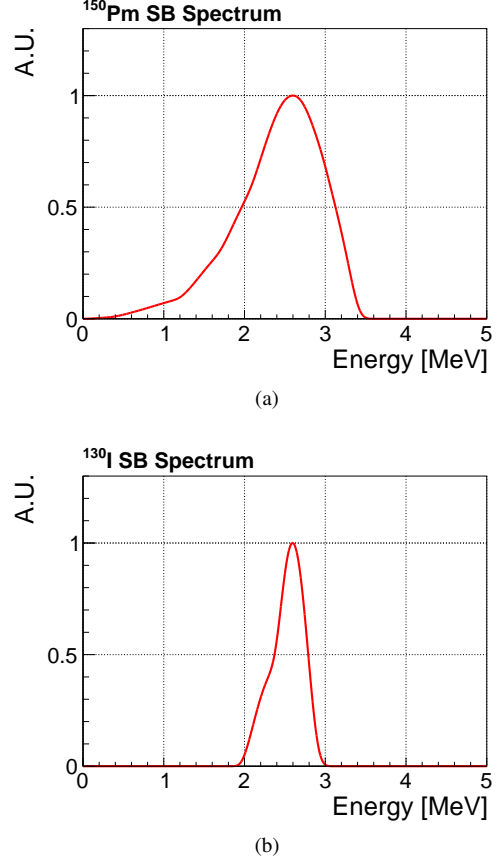


Fig. 4. The single beta (SB) energy spectra of (a) ${}^{150}\text{Pm}$ and (b) ${}^{130}\text{I}$ process, which come from the charged current process of ${}^{150}\text{Nd}$ and ${}^{130}\text{Te}$. The spectra are drawn with an energy resolution of $3\%/\sqrt{E(\text{MeV})}$.

C. Radioactive background

Radioactive isotopes in materials emit α , β and γ particles. These particles can deposit energy in the detector, contributing to the radioactive background. The primary isotopes that contribute to this background are those of the decay chains from ${}^{238}\text{U}$ and ${}^{232}\text{Th}$, along with the ${}^{40}\text{K}$ isotopes. The high energy γ from these sources, such as the 2.61 MeV γ of ${}^{208}\text{Tl}$, are capable of penetrating the detector materials and entering the detector center, depositing the energy to form background events. Table 1 shows the radioactive purity for various materials in the simulation.

Table 1. The radioactive purity of different detector materials used in the simulation.

Materials	^{238}U [g/g]	^{232}Th [g/g]	^{40}K [g/g]
Liquid scintillator[29]	1×10^{-16}	1×10^{-16}	1×10^{-18}
Acrylic[30]	6×10^{-13}	1.6×10^{-12}	null
Stainless steel [31]	3.7×10^{-10}	2.8×10^{-9}	4.5×10^{-7}
Water [29]	1×10^{-13}	2×10^{-13}	2×10^{-14}
PMT glass [29]	3×10^{-8}	1×10^{-8}	2×10^{-9}

D. Simulation for backgrounds

This research used the Monte Carlo (MC) method to simulate the $0\nu\beta\beta$ signals and $2\nu\beta\beta$, solar neutrino, and radioactive backgrounds. This method involves random sampling from the energy spectrum of each background to generate background events. The effect of energy resolution δ (ranging from $1\%/\sqrt{E(\text{MeV})}$ to $7\%/\sqrt{E(\text{MeV})}$) on the shape of the energy spectra is incorporated by convolving with a Gaussian function $N\left(\mu = 0, \sigma = \frac{\delta}{\sqrt{E(\text{MeV})}}\right)$.

For radioactive backgrounds, it is necessary to first obtain their visible energy (electron equivalent energy, unit is MeVee) spectra. To obtain these visible energy spectra, a detector simulation was conducted. In this detector simulation, for the isotope decay that occurs in the liquid scintillator, the ^{238}U decay chain, the ^{232}Th decay chain and ^{40}K were considered. For isotope decay that occurs outside the liquid scintillator, only specific nuclei were considered. These nuclei included ^{210}Tl , ^{214}Bi and ^{234}Pa in the ^{238}U decay chain, ^{208}Tl , ^{212}Bi and ^{228}Ac in the ^{232}Th decay chain and ^{40}K . The nuclei that would undergo α decay were not considered since the α particles would quench in the liquid scintillator and have low visible energy (<1.5 MeVee). Furthermore, nuclei with visible energies lower than 1.5 MeVee were not considered either, since they fall outside the fitting range (1.5~4.8 MeV). With the spectra of radioactive backgrounds, it is capable of performing MC simulations. As a sample, Fig. 5 shows the radioactive background energy spectra in the liquid scintillator (5-meter-radius sphere) with an energy resolution of $3\%/\sqrt{E(\text{MeV})}$.

As a result, Fig. 6 shows a sample of simulated background spectra of 1% natural Nd-loaded with an energy resolution of $3\%/\sqrt{E(\text{MeV})}$.

IV. COUNTING AND FITTING METHODS

The mathematical principles of the counting and fitting methods are described here, together with the fiducial volumes defined for both methods and the ROI selection of the counting method.

A. Counting method

The mathematical principles of the counting method are described in Section IV A 1. The fiducial volume and ROI selection for the counting method are described in Section IV A 2.

1. Mathematical principles of counting method

Based on the total number of events N_{ROI} observed in the ROI, the upper limit S_{limit} for the signal count at a given confidence level (C.L.) can be defined as

$$P(S_{\text{limit}} > S) \geq 1 - \alpha, \quad (5)$$

where the $1 - \alpha$ is the value of the confidence level.

For experiments with a large number of background events in the ROI, the Poisson distribution of N_{ROI} (i.e., $\pi(\lambda = B+S)$) can be approximated as a normal distribution: $N(\mu = B+S, \sigma^2 = B+S)$, where B and S are the expected numbers of background and signal in the ROI, respectively. Assuming the value of B is known in the experiment, the one-sided confidence interval for the estimate of the signal number \hat{S} can be obtained as [32]:

$$S_{\text{limit}} = N_{\text{ROI}} - B + n_{\sigma}\sqrt{N_{\text{ROI}}}, \quad (6)$$

where n_{σ} is corresponding to the confidence level. For example, a 90% confidence level ($\alpha = 0.1$) corresponds to a $n_{\sigma} = 1.28$.

With the number of signals much lower than the backgrounds, the equation (6) can be further approximated as:

$$S_{\text{limit}} = n_{\sigma}\sqrt{N_{\text{ROI}}}. \quad (7)$$

For a specific $0\nu\beta\beta$ isotope, the upper limit S_{limit} can be converted into the lower limit of the $0\nu\beta\beta$ half-life as following:

$$T_{1/2}^{\text{limit}} = \frac{N_A \times \ln 2}{n_{\sigma}\sqrt{N_{\text{ROI}}}} \frac{M_{\text{iso}} \times 10^6}{A_{\text{iso}}} \times t \times \epsilon, \quad (8)$$

where N_A is Avogadro's number, M_{iso} is the total mass of the $0\nu\beta\beta$ reaction isotope in the detector (in ton) and times the 10^6 to transfer into gram, A_{iso} is the atomic number of the isotope, t is the detector run time and ϵ is the detection efficiency.

By substituting $\Delta E \times b$ for N_{ROI} in (8), we have

$$T_{1/2}^{\text{limit}} = \frac{N_A \times \ln 2}{n_{\sigma}\sqrt{\Delta E \times b}} \frac{M_{\text{iso}} \times 10^6}{A_{\text{iso}}} \times t \times \epsilon, \quad (9)$$

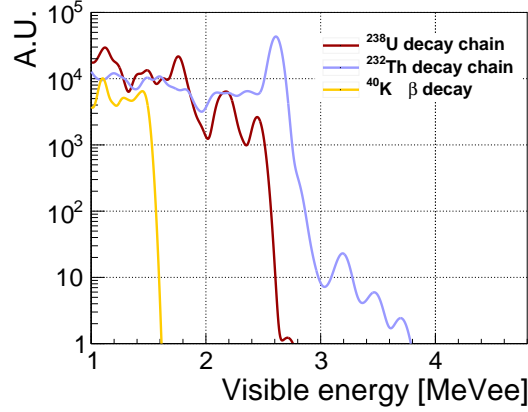


Fig. 5. Visible energy spectra of the radioactive backgrounds in liquid scintillator (5-meter-radius sphere) under a $3\%/\sqrt{E(\text{MeV})}$ energy resolution. For radioactive backgrounds in the liquid scintillator, the ^{238}U decay chain, the ^{232}Th decay chain and ^{40}K are considered. When outside the liquid scintillator, only a subset of nuclei are simulated, including ^{228}Ac , ^{212}Bi , ^{214}Bi , ^{234}Pa , ^{208}Tl , ^{210}Tl and ^{40}K .

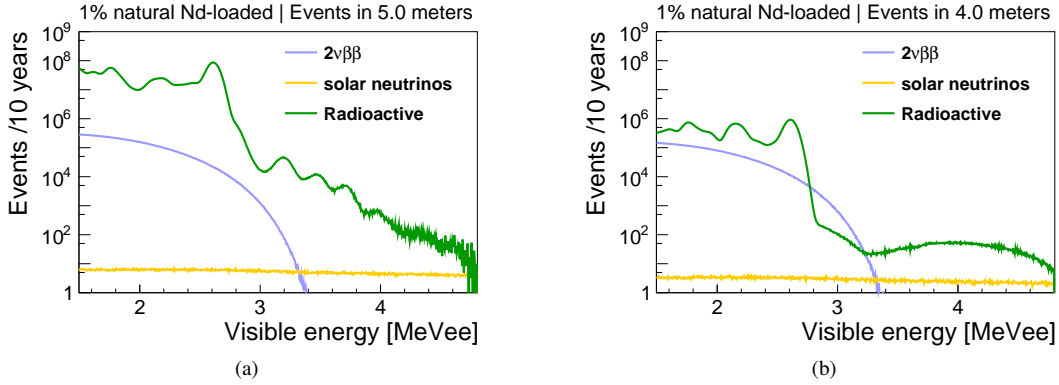


Fig. 6. A sample of simulated background spectra of 1% natural Nd-loaded within the (a) 5-meters-radius sphere and the (b) 4-meters-radius sphere. The energy resolution is set to $3\%/\sqrt{E(\text{MeV})}$.

where ΔE is the width of ROI and b is background count per energy unit. This equation can be used to estimate the sensitivity for an experiment [32].

2. Fiducial volume and ROI searching

Selecting the appropriate fiducial volume and the ROI range can enhance the sensitivity of the counting method. To determine the suitable fiducial volume and ROI, different values of them were tested, as described in detail below.

The radius was varied to optimize the fiducial volume with forty values ranging from 1.1 to 5.0 meters, with a step size of 0.1 meters. Additionally, as the fiducial volume reduced, an exponential decrease in the radioactive background originating from outside the liquid scintillator was observed. This reduction arises because the liquid scintillator outside the fiducial volume acts as a buffer layer. This reduction also leads to changes in the shape of the spectrum for different fiducial volumes, as shown in Fig. 6. Therefore, the spectral shape

for each fiducial volume condition was individually studied by simulating the radioactive backgrounds.

The selection of the ROI requires the determination of an appropriate ROI width and the center position of the ROI. To select a suitable ROI width, the ROI width ΔE_R , ranging from 0.02 to 1 MeV, was divided into fifty values with a step size of 0.02 MeV. Regarding the center position, the ROI was set as $[Q - 0.5\Delta E_R, Q + 0.5\Delta E_R]$, $[Q - 0.25\Delta E_R, Q + 0.75\Delta E_R]$ and $[Q, Q + \Delta E_R]$, since the $2\nu\beta\beta$ backgrounds are not symmetric near the Q -value.

The most suitable condition for the counting method was searched with an MC data set, and Fig. 7 shows the samples of the searching process. Then, for specific energy resolutions and isotopes, the fiducial volume radius and ROI corresponding to the highest 90% C.L. sensitivity were chosen. The fiducial volume and ROI selection results for the counting method are shown in Table 2.

As a result, the fiducial volume of ^{130}Te is smaller than that of ^{150}Nd because the radioactive backgrounds near the Q -value of ^{130}Te are much higher, so a smaller fiducial volume

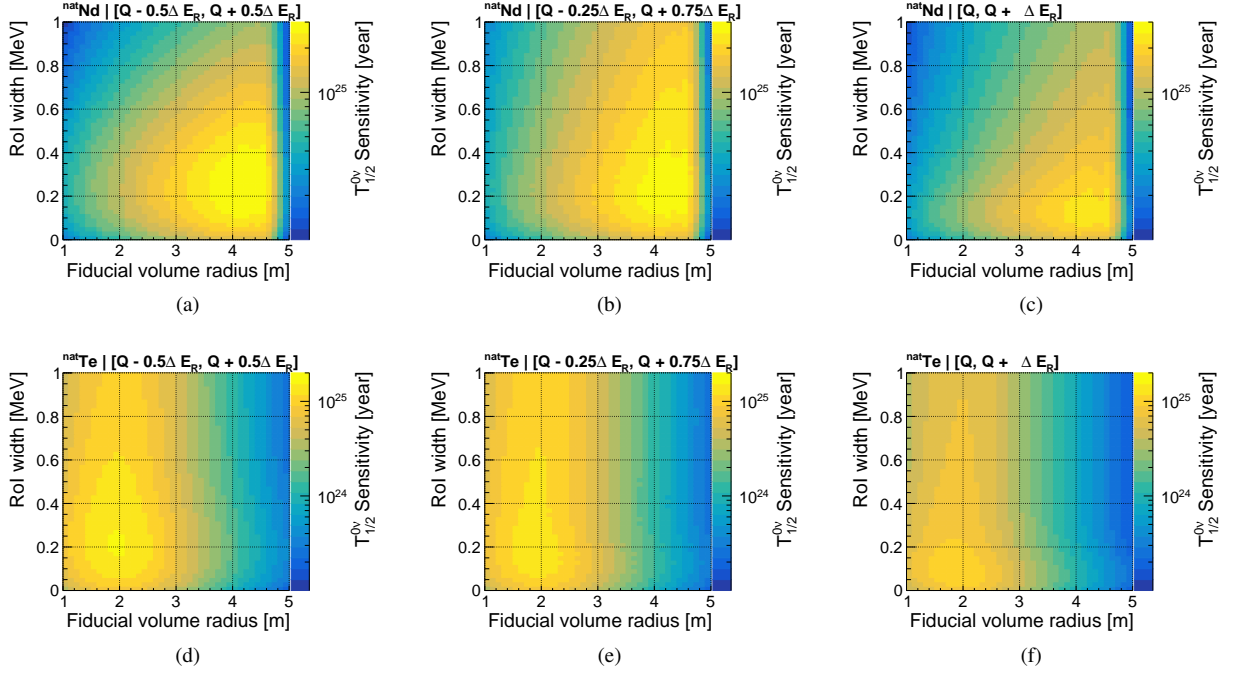


Fig. 7. The 90% C.L. sensitivities of $0\nu\beta\beta$ half-life vs. ROI width ΔE_R and fiducial volume radius, derived with 1% natural Nd-loaded (a,b,c) and 1% natural Te-loaded (d,e,f) under an energy resolution of $3\%/\sqrt{E}(\text{MeV})$ and a run time of 10 years (corresponding to the total exposure 2.85 ton-year for ^{150}Nd and 17.10 ton-year for ^{130}Te). The ROIs are set as $[Q - 0.5\Delta E_R, Q + 0.5\Delta E_R]$ for (a,d), $[Q - 0.25\Delta E_R, Q + 0.75\Delta E_R]$ for (b,e) and $[Q, Q + \Delta E_R]$ for (c,f).

Table 2. The fiducial volume and ROI selection for counting method with ^{150}Nd and ^{130}Te . The second column is the energy resolution δ , the third column is the radius of the fiducial volume, the fourth column is the ROI range and the fifth column is the exposure of the isotopes with the 1% natural Nd-loaded and 1% natural Te-loaded. The fiducial volume of ^{130}Te is smaller than that of ^{150}Nd because the radioactive backgrounds near the Q -value of ^{130}Te are much higher, so a smaller fiducial volume is needed to exclude these backgrounds.

Isotope	Energy resolution δ	Fiducial volume radius [m]	ROI range [MeV]	Exposure [ton-year]
^{150}Nd	0.01	4.6	$[3.35, 3.43]^2$	2.22
^{150}Nd	0.02	4.2	$[3.28, 3.45]^1$	1.69
^{150}Nd	0.03	4.3	$[3.25, 3.49]^1$	1.81
^{150}Nd	0.04	4.3	$[3.30, 3.59]^2$	1.81
^{150}Nd	0.05	4.6	$[3.27, 3.65]^2$	2.22
^{150}Nd	0.06	4.6	$[3.25, 3.72]^2$	2.22
^{150}Nd	0.07	4.6	$[3.37, 3.82]^3$	2.22
^{130}Te	0.01	2.3	$[2.50, 2.56]^1$	1.66
^{130}Te	0.02	2.2	$[2.46, 2.60]^1$	1.46
^{130}Te	0.03	2.1	$[2.42, 2.64]^1$	1.27
^{130}Te	0.04	2.0	$[2.37, 2.69]^1$	1.09
^{130}Te	0.05	2.0	$[2.31, 2.75]^1$	1.09
^{130}Te	0.06	2.1	$[2.26, 2.80]^1$	1.27
^{130}Te	0.07	2.1	$[2.24, 2.82]^1$	1.27

¹ ROI set as $[Q - 0.5\Delta E_R, Q + 0.5\Delta E_R]$.

² ROI set as $[Q - 0.25\Delta E_R, Q + 0.75\Delta E_R]$.

³ ROI set as $[Q, Q + \Delta E_R]$.

is needed to exclude these backgrounds.

B. Fitting method

The fitting method requires a detailed study of the background, and it is able to use events outside of the ROI. This research uses the Chi-squared (χ^2) fitting method. The form of the χ^2 function is described in Section IV B 1. The mathematical principle of the fitting method is described in Section IV B 2.

1. Chi-squared function

The fitting method used in this research utilizes a binned χ^2 fitting. The test statistic χ^2 consists of two components as

$$\chi^2 = \chi_{\text{energy}}^2 + \chi_{\text{penalty}}^2, \quad (10)$$

where

$$\chi_{\text{energy}}^2 = 2 \sum_{i=1}^{N_{\text{bin}}} \left(n_i \log \frac{n_i}{v_i} + v_i - n_i \right), \quad (11)$$

is a Poisson format χ^2 [33] and

$$\chi_{\text{penalty}}^2 = \sum_{k=1}^{N_{\text{bkg}}} \left(\frac{v_k^{\text{bkg}} - n_k^{\text{bkg}}}{\sigma_k^{\text{bkg}}} \right)^2, \quad (12)$$

where, N_{bin} denotes the number of bins in the fitting range, n_i is the observed number of events in the i -th bin, and $v_i = v_i^{\text{signal}} + \sum_k v_k^{\text{bkg}}$ is the expected number of events in the i -th bin, k represents for the k -th background. N_{bkg} denotes the number of background types, $v_k^{\text{bkg}} = \sum_{i=1}^{N_{\text{bin}}} v_{ki}^{\text{bkg}}$ represents the expected number of events of the k -th background, n_k^{bkg} represents its measured value and σ_k^{bkg} is the standard deviation of the measured value.

This research utilizes the TMINUIT class from the CERN ROOT [34] software package and employs its default optimization algorithm MIGRAD to minimize the χ^2 function. Fig. 8 shows a sample of χ^2 fitting with an energy resolution of $3\%/\sqrt{E}(\text{MeV})$ and a detector run time of 10 years (corresponding to the exposure of 1.35 ton-year for ^{150}Nd and 1.46 ton-year for ^{130}Te).

2. Mathematical principles of fitting method

The fitting method in this research used a binned χ^2 fitting method, and the Feldman-Cousins method [35] (FC method) is used to calculate confidence intervals. For a multi-dimensional sample, constructing a confidence band requires computationally intensive calculations and is difficult to visualize. Therefore, a toy MC method named profiled FC

method [36] was performed to solve this problem, which will be briefly introduced in the following.

For a specific value of the parameter $\mu = \mu_s$, multiple toy MC samples x_i will be generated, each corresponding to a $\Delta\chi_j^2(x_i; \mu_s) = \chi^2(x_i; \mu_s) - \chi^2(x_i; \mu_{\text{best}})$, where μ_{best} is the best fitting result of the parameter μ . Then, a certain value of $\Delta\chi_c^2(\mu_s)$ should be derived by making $1 - \alpha$ of toy MC samples satisfy $\Delta\chi_j^2(x_i; \mu_s) < \Delta\chi_c^2(\mu_s)$. After repeating this process for enough points of μ_s , one can get a curve of $\Delta\chi_c^2(\mu_s)$, then the confidence interval of μ for a specific sample x can be derived as:

$$I_\mu = \{\mu | \Delta\chi^2(x; \mu) < \Delta\chi_c^2(\mu)\}. \quad (13)$$

By performing the profiled FC method, one can avoid the construction of confidence bands in a multidimensional $x - \mu$ space. However, the profiled FC method still has the problem of choosing the values of the nuisance parameters during the toy MC generation process. One of the solutions is to pre-assign the values of the nuisance parameters to generate toy MC samples using a predetermined nuisance function [37].

In this research, the total count of each background $\{N_k\}$ and the $0\nu\beta\beta$ signal N_s were set as the fitting parameters, while the samples are the events in each bin $\{n_i\}$. The profiled FC method can be used to determine the confidence interval for the signal count N_s using the equation (13). In most situations, this confidence interval would encompass 0 and become an upper limit $N_{s|\text{upper}}$. This would allow for a straightforward conversion from an upper limit on the signal count $N_{s|\text{upper}}$ into a lower limit on the $0\nu\beta\beta$ half-life as $T_{\text{lower}}^{0\nu} = \frac{N_A \times \ln 2}{N_{s|\text{upper}}} \frac{M_{\text{iso}} \times 10^6}{A_{\text{iso}}} \times t \times \epsilon$, where the definitions of constants are the same as in equation (8).

Furthermore, in this research, this method is used to obtain the half-life sensitivity of $0\nu\beta\beta$. Sensitivity is obtained by generating toy MC samples with zero signal, calculating the $0\nu\beta\beta$ half-life lower limit for each MC sample, and choosing the median of the results.

3. Fiducial volume cut for fitting method

The fiducial volume cut searching for fitting method is same as the counting method described in Section IV A 2. Fig. 9 shows a sample of fiducial volume searching for the fitting method derived with ^{150}Nd and ^{130}Te , under an energy resolution of $3\%/\sqrt{E}(\text{MeV})$ and detector run time of 10 years, while the exposures of ^{150}Nd and ^{130}Te are change with the fiducial volume radius. Subsequently, for specific resolutions and isotopes, the fiducial volume radius corresponding to the highest 90% C.L. sensitivity of the $0\nu\beta\beta$ half-life was chosen. As a result, Table 3 gives the fiducial volume cuts.

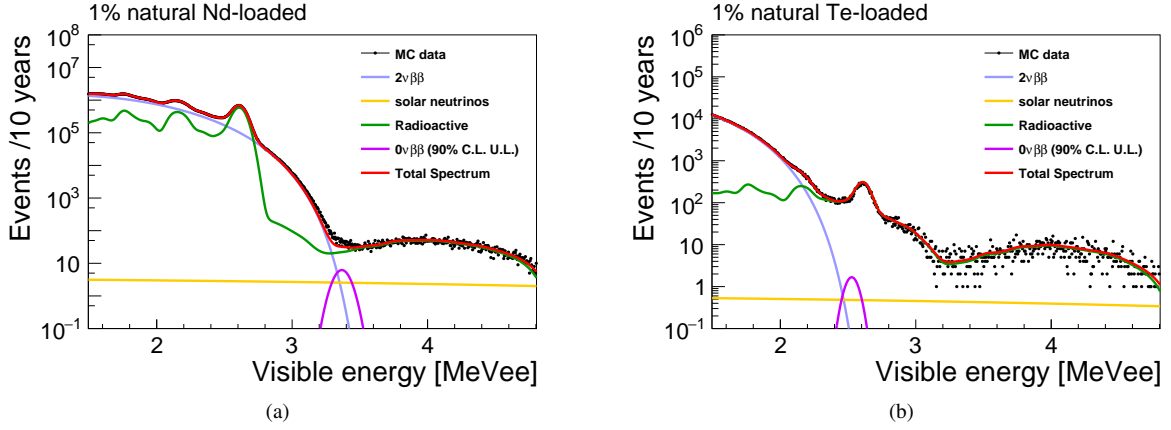


Fig. 8. Energy spectra of simulated events within the fiducial volume drawn together with best-fit backgrounds and the 90% C.L. upper limit for $0\nu\beta\beta$ of (a) 1% natural Nd-loaded in a 3.9-meter-radius sphere and (b) 1% natural Te-loaded in a 2.2-meter-radius sphere. The energy resolution is set to $3\%/\sqrt{E(\text{MeV})}$, detector run time is 10 years (corresponding to the exposure 1.35 ton-year for ^{150}Nd and 1.46 ton-year for ^{130}Te). Lines are fitting results and the black points are MC data.

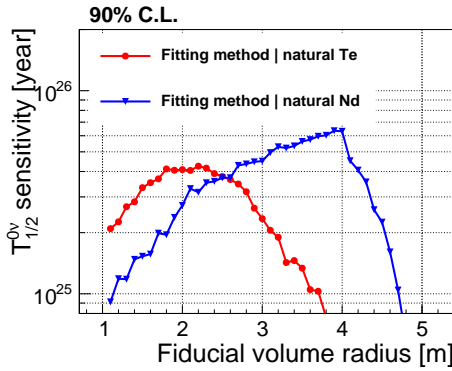


Fig. 9. A sample of fiducial volume search process for fitting method. The 90% C.L. sensitivities are derived with an energy resolution of $3\%/\sqrt{E(\text{MeV})}$ and a detector run time of 10 years. The red line is the result derived with 1% natural Te-loaded and the blue line is the result derived with 1% natural Nd-loaded.

C. Comparison of counting and fitting methods

The counting and fitting methods are compared by the obtained 90% C.L. sensitivities of the $0\nu\beta\beta$ half-life. The comparison was performed with different $0\nu\beta\beta$ isotopes (^{130}Te and ^{150}Nd) and different energy resolutions, while the other conditions are shown in Table 2 and Table 3. These half-life sensitivities were derived with optimal fiducial volume and ROI, and the results are shown in Fig. 10.

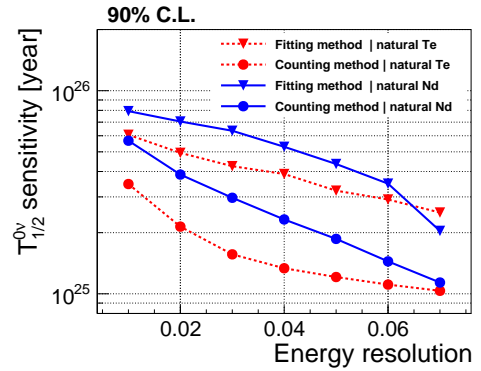


Fig. 10. The 90% C.L. sensitivity of $0\nu\beta\beta$ half-life of ^{130}Te and ^{150}Nd vs. energy resolution for fitting and counting methods. The red dashed lines are derived with 1% natural Te-loaded and the blue solid lines are derived with 1% natural Nd-loaded. Other conditions are shown in Table 2 and Table 3.

Under all energy resolution conditions used in this research, the fitting method achieves a higher sensitivity in the $0\nu\beta\beta$ half-life compared to the counting method.

For the fitting method, the sensitivity of the high Q -value isotope (^{150}Nd) shows a sharp decline when the energy resolution exceeds $6\%/\sqrt{E(\text{MeV})}$, and makes the sensitivity of the fitting method of ^{150}Nd lower than ^{130}Te at the energy resolution of $7\%/\sqrt{E(\text{MeV})}$. These phenomena are discussed in Section V B.

For the counting method, the sensitivity of the high Q -value isotope (^{150}Nd) decreases faster than that of the low Q -value isotope (^{130}Te). This is because the main background for the low Q -value isotope is the radioactivity background, while for the high Q -value isotope, its main background is the $2\nu\beta\beta$ background. The $2\nu\beta\beta$ background within the ROI will increase rapidly as the energy resolution deteriorates, leading to a faster decrease in sensitivity of the counting

Table 3. The fiducial volume cuts for fitting method with ^{150}Nd and ^{130}Te . The Second column is the energy resolution δ , the third column is the radius of the sphere corresponding to the fiducial volume bins and the fourth column is the exposure of the isotopes with the 1% natural Nd-loaded and 1% natural Te-loaded.

Isotope	Energy resolution δ	Fiducial volume radius [m]	Exposure [ton-year]
^{150}Nd	0.01	4.0	1.46
^{150}Nd	0.02	4.0	1.46
^{150}Nd	0.03	3.9	1.35
^{150}Nd	0.04	3.9	1.35
^{150}Nd	0.05	3.8	1.25
^{150}Nd	0.06	3.9	1.35
^{150}Nd	0.07	3.9	1.35
^{130}Te	0.01	2.1	1.27
^{130}Te	0.02	1.9	0.94
^{130}Te	0.03	2.2	1.46
^{130}Te	0.04	2.1	1.27
^{130}Te	0.05	1.9	0.94
^{130}Te	0.06	2.3	1.66
^{130}Te	0.07	1.8	0.80

method for the high Q -value isotope.

V. DISCUSSION

A. Comparison of effective neutrino mass obtained by different isotopes

For $0\nu\beta\beta$ experiments, the effective neutrino mass $\langle m_{\beta\beta} \rangle$ is also of greater interest, which satisfying the following relationship [38]

$$T_{1/2}^{0\nu-1} = G_{0\nu} g_A^4 |M_{0\nu}|^2 \left| \frac{\langle m_{\beta\beta} \rangle}{m_e} \right|^2, \quad (14)$$

where g_A is the coupling constant, m_e is the electron mass, and $G_{0\nu}$ and $M_{0\nu}$ are the phase space factor and nuclear matrix element related to the isotope, respectively. For the phase space factor $G_{0\nu}$, ^{150}Nd is around 4 times that of ^{130}Te [39], while for the nuclear matrix element $M_{0\nu}$, there is a large theoretical uncertainty [40–46].

As shown in Fig. 11, the 90% C.L. sensitivities of $\langle m_{\beta\beta} \rangle$ of ^{150}Nd are better than those of ^{130}Te in the same energy resolution, the method for sensitivity calculations and the model for the calculation of the nuclear matrix element (QRPA model and IBM model) [39]. As a result, for better $\langle m_{\beta\beta} \rangle$ sensitivity, natural Nd is a better choice than natural Te at the same loading mass fraction.

B. The sharp decline of sensitivity when fitting with Nd-150

The sensitivity of the fitting method with ^{150}Nd shows a sharp decline at the energy resolution $6\%/\sqrt{E(\text{MeV})}$, as

shown in Fig. 10. This feature arises from the $2\nu\beta\beta$ background of ^{150}Nd . As energy resolution deteriorates, the $2\nu\beta\beta$ background starts to overlap more and more $0\nu\beta\beta$ signals, leading to a significant drop in the performance of the fitting method, as shown in Fig. 12(a).

Fig. 12(b) shows the background events in $[Q - \sigma, Q + \sigma]$, where Q is the Q -value of ^{150}Nd and σ is the standard variation of the ^{150}Nd $0\nu\beta\beta$ signals. The background rate is indicated to increase rapidly with the deterioration of the energy resolution, providing evidence that $2\nu\beta\beta$ is an important factor that affects the sensitivity of ^{150}Nd .

The sharp decline of ^{150}Nd results in its sensitivity being lower than that of ^{130}Te at an energy resolution of $7\%/\sqrt{E(\text{MeV})}$. One of the reasons is that ^{150}Nd has more $2\nu\beta\beta$ background, and the other reason is that the natural abundance of ^{150}Nd (5.7%) is lower than that of ^{130}Te (34.2%).

VI. CONCLUSION

In this research, we focus on the comparison of counting and fitting method in $0\nu\beta\beta$ experiments. Based on simulation of a 500m^3 spherical liquid scintillator detector at CJPL, the $0\nu\beta\beta$ half-life sensitivities obtained from the counting and fitting methods were compared with an energy resolution of $1\%/\sqrt{E(\text{MeV})}$ to $7\%/\sqrt{E(\text{MeV})}$. We also performed a fiducial volume cut for both methods and checked the ROI selection for the counting method. Furthermore, ^{150}Nd and ^{130}Te were chosen as representations of isotopes of high Q and low Q values.

The results of this research indicate that the fitting method obtains a higher sensitivity than the counting method for the energy resolution of $1\%/\sqrt{E(\text{MeV})}$ to $7\%/\sqrt{E(\text{MeV})}$. Furthermore, this research shows that given the equivalent en-

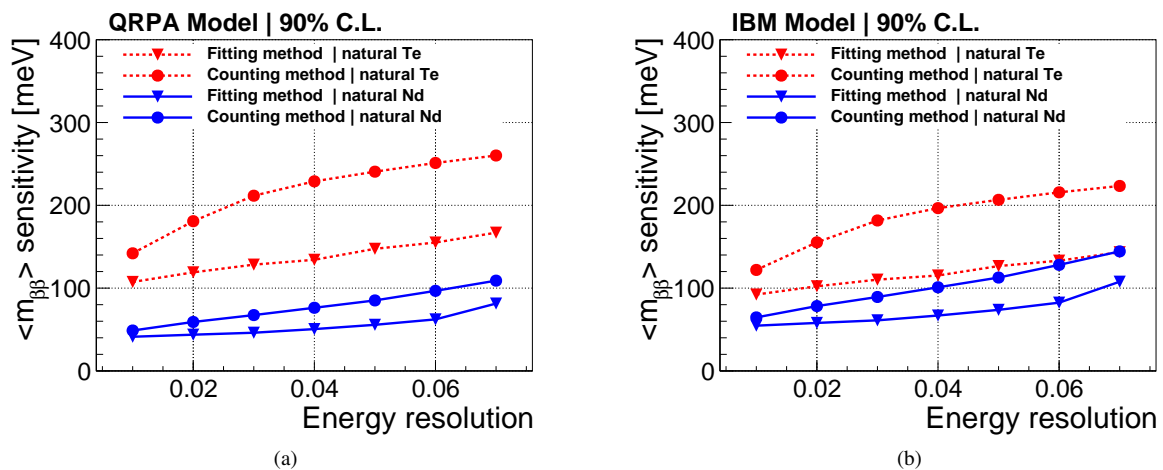


Fig. 11. The 90% C.L. sensitivities of effective neutrino mass vs. energy resolution. The red dashed lines are results derived with 1% natural Te-loaded and the blue solid lines are results derived with 1% natural Nd-loaded. The $G^{0\nu}$ and $M_{0\nu}$ are taken from QRPA model (a) and IBM model (b) data in Ref [39].

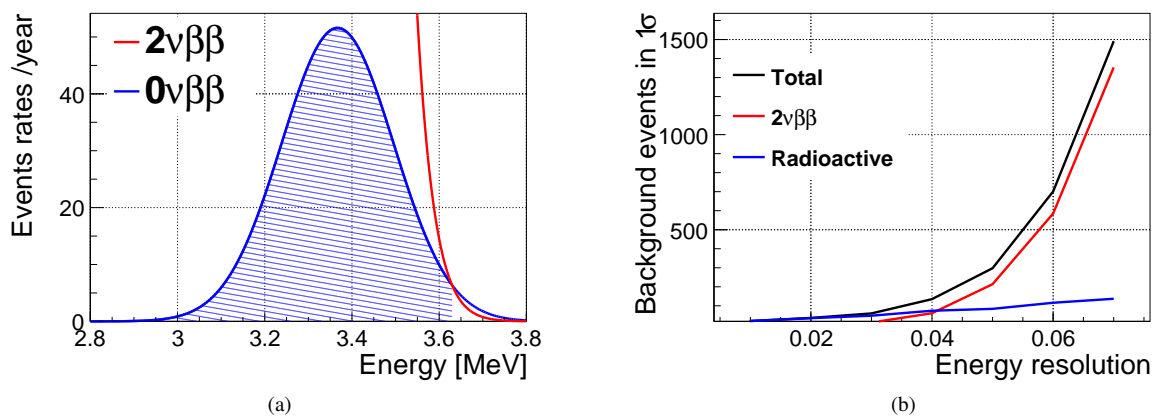


Fig. 12. (a) The ^{150}Nd $0\nu\beta\beta$ overlapped ratio drawn with an energy resolution of $7\%/\sqrt{E(\text{MeV})}$. The red line is the $2\nu\beta\beta$ background and the blue line is $0\nu\beta\beta$ signal. The dashed area is the overlapped $0\nu\beta\beta$ signals. The half-life of $0\nu\beta\beta$ is set at 5×10^{25} years, which is approximately the average sensitivity obtained in Section IV C. (b) The background events in one year for 1% natural Nd-loaded in the energy range $[Q - \sigma, Q + \sigma]$, where Q is the Q -value of $0\nu\beta\beta$ and σ is standard variation of $0\nu\beta\beta$ signals. The solar neutrino background is neglected, since they are much smaller than the other backgrounds.

energy resolution, run time, and loading mass fraction, the effective neutrino mass $\langle m_{\beta\beta} \rangle$ derived from natural Nd is lower than that derived from natural Te. This research could provide guidance for future experiments in selecting the appropriate method for sensitivity calculations and $0\nu\beta\beta$ isotopes.

We chose the energy resolution of $3\%/\sqrt{E(\text{MeV})}$ as a typical value of the liquid scintillator detector. Under this energy resolution and an exposure of 1.35 ton-year for ^{150}Nd and 1.46 ton-year for ^{130}Te , the better sensitivity comes from

the fitting method, as

$$^{150}\text{Nd} : 6.34 \times 10^{25} \text{ yr (90\% C.L.)}$$

$$^{130}\text{Te} : 4.50 \times 10^{25} \text{ yr (90\% C.L.)}$$

These $0\nu\beta\beta$ half-life correspond to the effective neutrino mass $\langle m_{\beta\beta} \rangle$ 43-93 meV for ^{150}Nd and 76-150 meV for ^{130}Te .

- doi:10.1146/annurev-nucl-101918-023407
- [2] W. Rodejohann, Neutrino-less double beta decay and particle physics. *Int. J. Mod. Phys. E* **20**, 1833–1930 (2011). [arXiv:1106.1334](#), doi:10.1142/S0218301311020186
- [3] Z. Zeng, Y.H. Mi, M. Zeng, et al., Characterization of a broad-energy germanium detector for its use in cjpl. *Nucl. Sci. Tech.* **28**, 7 (2017). doi:10.1007/s41365-016-0162-y
- [4] W.H. Dai, et al., Search for neutrinoless double-beta decay of ^{76}Ge with a natural broad energy germanium detector. *Phys. Rev. D* **106**, 032012 (2022). [arXiv:2205.10718](#), doi:10.1103/PhysRevD.106.032012
- [5] I. Nutini, et al., Latest results from the cuore experiment. *J. Low Temp. Phys.* **209**, 927–935 (2022). doi:10.1007/s10909-022-02873-y
- [6] E. Armengaud, et al., New limit for neutrinoless double-beta decay of ^{100}Mo from the cupid-mo experiment. *Phys. Rev. Lett.* **126**, 181802 (2021). [arXiv:2011.13243](#), doi:10.1103/PhysRevLett.126.181802
- [7] W. Chen, L. Ma, J.H. Chen, et al., Gamma-, neutron-, and muon-induced environmental background simulations for ^{100}Mo -based bolometric double-beta decay experiment at jinning underground laboratory. *Nucl. Sci. Tech.* **34**, 135 (2023). [arXiv:2206.09288](#), doi:10.1007/s41365-023-01299-9
- [8] M. Agostini, et al., Final results of gerda on the search for neutrinoless double- β decay. *Phys. Rev. Lett.* **125**, 252502 (2020). [arXiv:2009.06079](#), doi:10.1103/PhysRevLett.125.252502
- [9] X. Yan, et al., Searching for two-neutrino and neutrinoless double beta decay of ^{134}Xe with the pandax-4t experiment. *Phys. Rev. Lett.* **132**, 152502 (2024). [arXiv:2312.15632](#), doi:10.1103/PhysRevLett.132.152502
- [10] W. Feldmeier, Search for neutrinoless double beta decay in ^{136}Xe with exo-200. Ph.D. thesis, Munich, Tech. U. (2015)
- [11] A. Gando, et al., Search for majorana neutrinos near the inverted mass hierarchy region with kamland-zen. *Phys. Rev. Lett.* **117**, 082503 (2016). [Addendum: *Phys.Rev.Lett.* **117**, 109903 (2016)]. [arXiv:1605.02889](#), doi:10.1103/PhysRevLett.117.082503
- [12] S. Abe, et al., Search for the majorana nature of neutrinos in the inverted mass ordering region with kamland-zen. *Phys. Rev. Lett.* **130**, 051801 (2023). [arXiv:2203.02139](#), doi:10.1103/PhysRevLett.130.051801
- [13] X.G. Cao, et al., N_{ν} dex-100 conceptual design report. *Nucl. Sci. Tech.* **35**, 3 (2024). [arXiv:2304.08362](#), doi:10.1007/s41365-023-01360-7
- [14] C.F. Yang, Y.B. Huang, J.L. Xu, et al., Reconstruction of a muon bundle in the jun0 central detector. *Nucl. Sci. Tech.* **33**, 59 (2022). [arXiv:2201.11321](#), doi:10.1007/s41365-022-01049-3
- [15] Y.Y. Ding, M.C. Liu, L.J. Wen, et al., A novel approach in synthesizing te-diol compounds for tellurium-loaded liquid scintillator. *Nucl. Instrum. Meth. A* **1049**, 168111 (2023). doi:10.1016/j.nima.2023.168111
- [16] V. Albanese, et al., The sno+ experiment. *JINST* **16**, P08059 (2021). [arXiv:2104.11687](#), doi:10.1088/1748-0221/16/08/P08059
- [17] I.R. Barabanov, et al., Searches for neutrinoless double-beta decay of the isotope ^{150}Nd by means of a liquid organic scintillator detector. *Phys. Atom. Nucl.* **82**, 89–97 (2019). doi:10.1134/S1063778819020029
- [18] W. Luo, Q. Liu, Y. Zheng, et al., Reconstruction algorithm for a novel cherenkov scintillation detector. *JINST* **18**, P02004 (2023). [arXiv:2209.13772](#), doi:10.1088/1748-0221/18/02/P02004
- [19] Z. Guo, et al., Muon flux measurement at china jinning underground laboratory. *Chin. Phys. C* **45**, 025001 (2021). [arXiv:2007.15925](#), doi:10.1088/1674-1137/abccae
- [20] W.H. Zeng, H. Ma, M. Zeng, et al., Evaluation of cosmogenic activation of copper and germanium during production in jinning underground laboratory. *Nucl. Sci. Tech.* **31**, 50 (2020). doi:10.1007/s41365-020-00760-3
- [21] K. Zuber, *Neutrino Physics*, (Taylor & Francis, Boca Raton, 2020). doi:10.1201/9781315195612
- [22] H. Primakoff, S.P. Rosen, Double beta decay. *Rept. Prog. Phys.* **22**, 121–166 (1959). doi:10.1088/0034-4885/22/1/305
- [23] A. Serenelli, Alive and well: a short review about standard solar models. *Eur. Phys. J. A* **52**, 78 (2016). [arXiv:1601.07179](#), doi:10.1140/epja/i2016-16078-1
- [24] S.M. Bilenky, Neutrino masses, mixing and oscillations. *Prog. Part. Nucl. Phys.* **57**, 61–67 (2006). [arXiv:hep-ph/0510175](#), doi:10.1016/j.pnpnp.2005.10.001
- [25] L. Baudis, A. Ferella, A. Kish, et al., Neutrino physics with multi-ton scale liquid xenon detectors. *JCAP* **01**, 044 (2014). [arXiv:1309.7024](#), doi:10.1088/1475-7516/2014/01/044
- [26] H. Ejiri, S.R. Elliott, Solar neutrino interactions with the double beta decay nuclei of ^{82}Se , ^{100}Mo and ^{150}Nd . *Phys. Rev. C* **95**, 055501 (2017). [arXiv:1703.06915](#), doi:10.1103/PhysRevC.95.055501
- [27] H. Ejiri, S.R. Elliott, Charged current neutrino cross section for solar neutrinos, and background to $\beta\beta(0\nu)$ experiments. *Phys. Rev. C* **89**, 055501 (2014). [arXiv:1309.7957](#), doi:10.1103/PhysRevC.89.055501
- [28] E.J. Konopinski, Beta-Decay,. *Rev. Mod. Phys.* **15**, 209–245 (1943). doi:10.1103/RevModPhys.15.209
- [29] C. Arpesella, et al., Measurements of extremely low radioactivity levels in borexino. *Astropart. Phys.* **18**, 1–25 (2002). [arXiv:hep-ex/0109031](#), doi:10.1016/S0927-6505(01)00179-7
- [30] SNO collaboration, Sno technical reports. (2022) <https://sno.phy.queensu.ca/str/rad.html>
- [31] G. Hussain, Z. Zeng, C. Yao, et al., Assay of low-background stainless steel by smelting for the neutrino experiment at jinning. *Nucl. Instrum. Meth. A* **881**, 65–71 (2018). [arXiv:1706.04506](#), doi:10.1016/j.nima.2017.11.006
- [32] S. Dell’Oro, S. Marcocci, M. Viel, et al., Neutrinoless double beta decay: 2015 review. *Adv. High Energy Phys.* **2016**, 2162659 (2016). [arXiv:1601.07512](#), doi:10.1155/2016/2162659
- [33] X. Ji, W. Gu, X. Qian, et al., Combined neyman–pearson chi-square: An improved approximation to the poisson-likelihood chi-square. *Nucl. Instrum. Meth. A* **961**, 163677 (2020). [arXiv:1903.07185](#), doi:10.1016/j.nima.2020.163677
- [34] R. Brun, F. Rademakers, Root: An object oriented data analysis framework. *Nucl. Instrum. Meth. A* **389**, 81–86 (1997). doi:10.1016/S0168-9002(97)00048-X
- [35] G.J. Feldman, R.D. Cousins, A unified approach to the classical statistical analysis of small signals. *Phys. Rev. D* **57**, 3873–3889 (1998). [arXiv:physics/9711021](#), doi:10.1103/PhysRevD.57.3873
- [36] T.M. Karbach, Feldman-cousins confidence levels - toy mc method. *arXiv preprint arXiv:1109.0714* . [arXiv:1109.0714](#)
- [37] M.A. Acero, et al., The profiled feldman-cousins technique for confidence interval construction in the presence of nuisance parameters. *arXiv preprint arXiv:2207.14353* . [arXiv:2207.14353](#)
- [38] F.T. Avignone, III, S.R. Elliott, J. Engel, Double beta decay, majorana neutrinos, and neutrino mass. *Rev. Mod. Phys.* **80**, 481–516 (2008). [arXiv:0708.1033](#), doi:10.1103/RevModPhys.80.481

- [39] R.G.H. Robertson, Empirical survey of neutrinoless double beta decay matrix elements. *Mod. Phys. Lett. A* **28**, 1350021 (2013). [arXiv:1301.1323](#), [doi:10.1142/S0217732313500211](#)
- [40] J. Menendez, A. Poves, E. Caurier, et al., Disassembling the nuclear matrix elements of the neutrinoless beta beta decay. *Nucl. Phys. A* **818**, 139–151 (2009). [arXiv:0801.3760](#), [doi:10.1016/j.nuclphysa.2008.12.005](#)
- [41] J. Barea, F. Iachello, Neutrinoless double-beta decay in the microscopic interacting boson model. *Phys. Rev. C* **79**, 044301 (2009). [doi:10.1103/PhysRevC.79.044301](#)
- [42] T.R. Rodriguez, G. Martinez-Pinedo, Energy density functional study of nuclear matrix elements for neutrinoless $\beta\beta$ decay. *Phys. Rev. Lett.* **105**, 252503 (2010). [arXiv:1008.5260](#), [doi:10.1103/PhysRevLett.105.252503](#)
- [43] P.K. Rath, R. Chandra, K. Chaturvedi, et al., Uncertainties in nuclear transition matrix elements for neutrinoless $\beta\beta$ decay within the phfb model. *Phys. Rev. C* **82**, 064310 (2010). [arXiv:1104.3965](#), [doi:10.1103/PhysRevC.82.064310](#)
- [44] F. Simkovic, A. Faessler, H. Muther, et al., The $0\nu\beta\beta$ -decay nuclear matrix elements with self-consistent short-range correlations. *Phys. Rev. C* **79**, 055501 (2009). [arXiv:0902.0331](#), [doi:10.1103/PhysRevC.79.055501](#)
- [45] D.L. Fang, A. Faessler, V. Rodin, et al., Neutrinoless double-beta decay of ^{150}Nd accounting for deformation. *Phys. Rev. C* **82**, 051301 (2010). [arXiv:1009.5579](#), [doi:10.1103/PhysRevC.82.051301](#)
- [46] O. Civitarese, J. Suhonen, Nuclear matrix elements for double beta decay in the qrpa approach: A critical review. *J. Phys. Conf. Ser.* **173**, 012012 (2009). [doi:10.1088/1742-6596/173/1/012012](#)